JACS
JOURNAL OF THE AMERICAN CHEMICAL SOCIETY

Article

pubs.acs.org/JACS

Membrane Permeation versus Amyloidogenicity: A Multitechnique Study of Islet Amyloid Polypeptide Interaction with Model Membranes

Anne Martel,*[,†] Lucas Antony,[‡] Yuri Gerelli,[†] Lionel Porcar,[†] Aaron Fluitt,[‡] Kyle Hoffmann,[‡] Irena Kiesel,[†] Michel Vivaudou,[§] Giovanna Fragneto,[†] and Juan J. de Pablo[‡]

[†]The Institut Laue Langevin, 38042 Grenoble, France

[‡]Institute for Molecular Engineering, University of Chicago, Chicago, Illinois 60637, United States

[§]Institut de Biologie Structurale (IBS), University Grenoble Alpes, CEA, CNRS, 38044 Grenoble, France

Supporting Information

ABSTRACT: Islet amyloid polypeptide (IAPP) is responsible for cell depletion in the pancreatic islets of Langherans, and for multiple pathological consequences encountered by patients suffering from type 2 Diabetes Mellitus. We have examined the amyloidogenicity and cytotoxic mechanisms of this peptide by investigating model-membrane permeation and structural effects of fragments of the human IAPP and several rat IAPP mutants. In vitro experiments and molecular dynamics simulations reveal distinct physical segregation, membrane permeation, and amyloid aggregation processes that are mediated by two separate regions of the peptide. These observations suggest a "detergent-like" mechanism, where lipids are extracted from the bilayer by the N-terminus of IAPP, and integrated into amyloid aggregates. The amyloidogenic aggregation would kinetically compete with the process of membrane permeation and, therefore, inhibit it. This hypothesis represents a new perspective on the mechanism underlying the membrane disruption by amyloid peptides, and could influence the development of new therapeutic strategies.

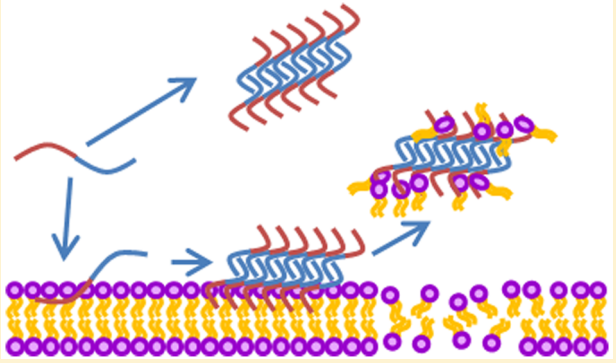

INTRODUCTION

Amyloidoses are an ensemble of diseases commonly characterized by the presence of large insoluble aggregates of protein fibers in key organs. Disease symptoms are thought to arise from abnormal cell death in regions where these aggregates are localized. For instance, in Alzheimer's disease, amyloidal plaques are localized in the brain, where dramatic neuronal losses explain many symptoms of senility. For each disease, the main constituent of these aggregates is a specific peptide: the aβ peptide in Alzheimer's disease, the α-synuclein peptide in Parkinson's disease, the prion peptide in Creuztfeld–Jacob's disease, etc. Although these peptides have different sequences, they all exhibit the ability to adopt an extremely stable fibrillar structure characterized by cross β-sheet folds, which is the defining structure of amyloid fibers. The colocalization of fibrillar aggregates with cell depletion, and the structural similarities between all amyloid fibers, lead to the hypothesis that these fibrils or aggregates are the cytotoxic species responsible for the onset of symptoms. Note, however, that cell viability experiments have shown that preformed fibers are not cytotoxic,[1] thereby leading to the suggestion that the toxicity is either coming from prefibrillar structures, or that the process of fibrillation itself triggers cell apoptosis. In the first hypothesis, the specific peptide would fold and assemble into a toxic small aggregate or oligomer consisting of several molecules.[2−6] That aggregate would get embedded into the membrane and, possibly, form a pore. This oligomer could be an intermediate along the fiber formation pathway, but whether or not this is the case has not been clarified for all peptides. In the second hypothesis, the growth of the fibers would distort the membrane of neighboring cells and severely affect their cellular function.[7]

The existence of a common cytotoxicity mechanism for all the amyloid diseases is generally accepted, whereby damage to some cell membranes disrupts ionic homeostasis.[2,8] What is not known, however, is which membrane is the target of this permeation (cytoplasmic or organelle membranes), and how an amyloid peptide interacts with its target membrane. These issues continue to be the subject of debate, although some authors have proposed that the membrane permeation caused by various amyloid peptides implies the formation of an oligomeric pore.[9] Given the multitude of controversial observations published through decades of research on amyloids, it might be that different amyloid peptides act

Received: July 6, 2016
Published: December 6, 2016

DOI: 10.1021/jacs.6b06985
J. Am. Chem. Soc. 2017, 139, 137−148

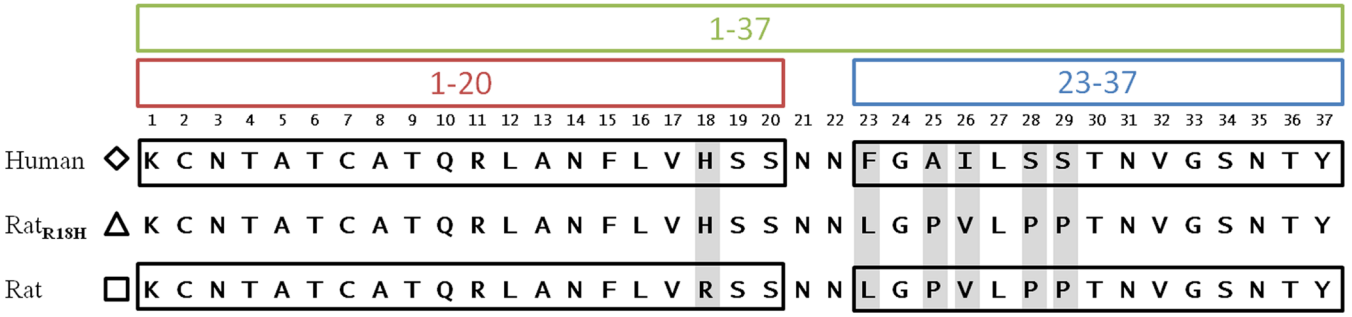

Figure 1. Sequence of the peptides used in this study: the hIAPP$_{1-37}$: the human peptide (top) and the rIAPP$_{1-37}$, the rat peptide (bottom) are split in two fragments: the N-terminal from amino acid 1 to 20 (hIAPP$_{1-20}$ and rIAPP$_{1-20}$) and the C-terminal from amino acid 23 to 37 hIAPP$_{23-37}$ and rIAPP$_{23-37}$). The mismatches between the human and rat sequences are highlighted in gray. The sequence of the chimeric peptide rIAPP$_{1-37}$R18H is in the middle.

differently and that amyloid peptides may be able to disrupt the membrane through several processes.[10]

The current study aims to enrich our knowledge of the cytotoxic mechanism of IAPP, the Islet Amyloid PolyPeptide (also named Amylin), which is implicated in type 2 Diabetes Mellitus (T2DM).[11] This 37-amino acid long peptide is a hormone cosecreted with insulin by the β-cells of the islets of Langherans in the pancreas. Under healthy conditions, it is produced in lower amounts than insulin; however, its rate of production increases strikingly during disease development. Furthermore, it is the main constituent of the amyloid aggregates found in the pancreas of T2DM patients near sites of β-cell depletion. Significant efforts have sought to understand the mechanism of β-cell death induced by IAPP. It is likely that IAPP, like other amyloid peptides, induces apoptosis by disrupting ionic homeostasis, but the mechanism of membrane permeation is still not clear and several different hypotheses exist today.[8,12,13] These include the following:

(i) The "oligomeric pore" hypothesis, in which IAPP self-assembles into a transient toxic oligomer that interacts with the cell membrane and forms a pore. This oligomer is possibly an intermediate structure along the fiber formation pathway.[14] It could exist as a transient entity rather than a stable assembly.[14]

(ii) The "detergent-like" hypothesis stipulates that IAPP extracts lipids from the bilayer and integrates them into self-assembling micellar objects or in the amyloid fibrils.[15] Depletion of the first leaflet lipids would cause a thinning of the membrane,[13] resulting in permeability to ions.

(iii) The "non-specific" hypothesis explains the membrane disruption as a consequence of mechanical pressure induced by fibril growth at the surface of the membrane.[7,16]

This study seeks to correlate structural and functional data recorded by in vitro assays conducted under comparable conditions, and interpret them using molecular simulations, in order to gain insights into the mechanism of amyloid toxicity. Our strategy has been influenced by two main publications: In 2003, Green and co-workers reported that, by mutating a single position of the nontoxic and nonamyloidogenic rat IAPP, the peptide acquired both cytotoxic properties and a propensity for amyloid aggregation.[17] This observation strongly suggests that amyloidogenicity and cytotoxicity are linked by a causal relationship. Some of our recent computational work has confirmed that such mutations increase the ability of the peptide to form beta sheets and small aggregates.[18] In 2008, Brender and co-workers reported that the amyloidogenic propensity and the cytotoxic properties of human IAPP were independent of each other and enabled by distinct regions within the peptide sequence.[19] The present study shows how both statements can be reconciled, and provides new insight into amyloid aggregation.

In addition to considering the full-length human IAPP peptide (hIAPP$_{1-37}$), in this study IAPP was also split into two fragments (Figure 1) in an attempt to decouple membrane interaction and amyloidogenicity:[19]

- The amino-terminal half (from amino acid 1 to 20): hIAPP$_{1-20}$ is expected to be involved in the interaction between the peptide and the lipid bilayer.[20]
- The carboxy-terminal half (from amino acid 23 to 37): hIAPP$_{23-37}$ is considered strongly amyloidogenic, since it constitutes the "spine" of amyloid fibers.[21]
- The full-length rat peptide (rIAPP$_{1-37}$) and its fragments (rIAPP$_{1-20}$, rIAPP$_{23-37}$) are used as nontoxic and nonamyloidogenic controls.[19]
- The rat mutant rIAPP$_{1-37}$R18H, where the arginine in position 18 is mutated to histidine like that in the human peptide, can be considered as a chimeric peptide joining the human N-terminal half to the rat C-terminal half. Indeed, the amino acid at position 18 is the only difference between the rat and the human peptides within the N-terminal half of their sequences. The other five differences are located in the C-terminal half of the molecule.

Due to amino acids 21 and 22 being identical in the rat and human peptides, they are considered as nonessential for the cytotoxicity and amyloidogenicity of IAPP and excluded from the peptide fragments.

To further decouple the effects from amyloidogenicity and membrane interactions, we also conducted extensive molecular simulations of single IAPP fragments in the immediate vicinity of a model lipid bilayer. Specifically, we compared the interactions of hIAPP$_{1-20}$, rIAPP$_{1-20}$, and hIAPP$_{23-37}$ with a model phospholipid bilayer. By focusing on single peptide interactions, one can eliminate the confounding effects of aggregation and work with a computationally tractable model that retains fine structural information. Such an approach also affords an opportunity to examine the membrane interactions of the N- and C-terminal sequences of IAPP independently.

DOI: 10.1021/jacs.6b06985
J. Am. Chem. Soc. 2017, 139, 137−148

MATERIALS AND METHODS

Materials. Dimethyl-sulfoxide deuterated in six positions (DMSO-d_6) was purchased from EurIsotop, lipids from Avanti Polar lipids and the other chemicals from Sigma-Aldrich. The buffer used in all measurements consists of 100 mM Hepes, 150 mM NaCl and set to pH 7.4, except in circular dichroism measurements where it was replaced by a 100 mM phosphate, 150 mM NaF pH 7.4 buffer.

All of the peptides were chemically synthesized and purified by CsBio (human fragments) and Anatech (rat fragments). Their purity was checked by mass spectrometry. The post-translation modifications were reproduced: position 37 amidation[12] and a disulfide bond between cysteines in positions 2 and 7. These modifications were taken into account during all calculations. Upon reception, the peptides were dissolved in DMSO-d_6 containing 0.1% trifluoroacetic acid to a stock concentration of 1.4 mM, aliquoted and flash-frozen in liquid nitrogen. This stock solution was stored at −20 °C.

To mimic a fluid cell membrane, 1-palmitoyl-2-oleoyl-*sn*-glycero-3-phosphocholine (POPC) lipid was used. POPC consists of a phosphatidylcholine zwitterionic headgroup, a 16 carbon long saturated aliphatic chain, and an 18 carbon long aliphatic chain that is unsaturated on C9. Several aspects of the cell membrane are modeled in terms of headgroup charges, aliphatic chain unsaturation and chain lengths. Its partially deuterated version (D_{31}-POPC) carries 31 nonlabile deuterium atoms on its palmitoyl chain.

Amyloidogenicity Prediction. Three pieces of software were used to predict the probability of hIAPP and rIAPP residues to form amyloid structure: Tango[22] (http://tango.crg.es/), Aggrescan[23] (http://bioinf.uab.es/aap/) and ZipperDB[24] (http://services.mbi.ucla.edu/zipperdb/intro). They were chosen for their diversity in approach and for their ease of use. Tango predicts the probability of each amino acid to be part of an amyloidogenic sequence based on its physicochemical characteristics. ZipperDB predicts the propensity of a hexapeptide (sliding along the sequence of interest) to form β-zipper structures by using molecular dynamics and potential energy calculations. Aggrescan detects aggregation hotspots within the sequence of interest using a score of aggregation propensity empirically obtained for each amino acid by analyzing a wide set of proteins.

Dynamic Light Scattering (DLS). The diffusion coefficient of a particle in suspension was calculated using DLS. Assuming the solution viscosity stays constant, the diffusion coefficient is directly related to the size of the particles. Diffusion measurements were carried out on the ALV system available at the Partnership for Soft Condensed Matter (PSCM), Institut Laue-Langevin (ILL, Grenoble, France). The sample consisted of 9.2 μL of peptide stock solution diluted in 460 μL of buffer. Starting from the diluted sample, 120 correlation functions, each with 30 s exposure time, were recorded at an angle of 90 deg with respect to the incident beam. The correlation functions recorded within 1 min after dilution, and subsequently after 5, 10, 30, and 60 min, are presented. The autocorrelation curves have been fitted using a double stretched exponential model to extract a population distribution as in reference.[25]

Thioflavin T (ThT) Fluorescent Assays. Thioflavin T is a dye that displays enhanced fluorescence and a red shift when inserted between pleated β-sheets. It is widely used as a marker for amyloid aggregates. The fluorimetric assays were carried our using a plate-reader where 2 μL of sample stock solution was diluted with 100 μL of buffer containing 1 mg/mL of POPC vesicles, in a nonbinding polystyrene 96-well plate (Corning 3881). The excitation wavelength was set to 350 nm and the measured one to 453 nm. Spectra were recorded every 10 min for 17 hours.

Circular Dichroism (CD). CD calculates ellipticity spectra, which are used to estimate the secondary structure of a protein.[26] Samples were diluted to a concentration of 27.5 μM in 10 μM phosphate buffer at pH 7.4 containing 150 mM NaF, to mimic the usual buffer with chemicals deprived of circular dichroism signal, and incubated 6 h at room temperature. They were then freeze-dried to remove DMSO and resuspended in water before measurement. The samples' ellipticity was measured on a Jasco instrument (Biophysics platform: Partnership for Structural Biology, Grenoble, France) in 2 mm path length quartz cuvettes.

Membrane Conductance Measurements. Membrane conductance measurements were performed using droplet-interface bilayers following the protocol described by Syeda et al.,[27] in the "lipid out" version described by Bayley et al.,[28] on a dedicated instrument available at the PSCM. Briefly, a POPC monolayer spontaneously organizes at the surface of two droplets of aqueous buffer immersed in hexadecane containing 0.5 mg/mL of POPC. Bringing the two droplets together results in the formation of a POPC bilayer at their interface. An electrode is immersed within each droplet to apply voltage and record the current passing through the bilayer using an electrophysiology amplifier (AM system, Model 2400) in voltage-clamp mode.

Neutron Reflectometry (NR). Reflectometry experiments were performed on FIGARO,[29] the horizontal-surface reflectometer at the Institut Laue Langevin. The lipid bilayers were deposited on a silicon crystal by vesicle fusion using calcium chloride 1 M, and placed on top of the buffer chamber. First the silicon crystals were characterized to define the structure of the native oxide layer on their surface. The lipid bilayers were then characterized before and after peptide injection by varying the D_2O/H_2O ratio of the buffer. The peptide stock solution was flanked by pure DMSO during injection. By this mean, the peptide got diluted in aqueous buffer only once it reached the bilayer chamber. The data were reduced using Lamp software (ILL) and fitted using Aurore.[30]

Small Angle Neutron Scattering. Small Angle Neutron Scattering experiments were carried out using the D22 diffractometer at the ILL. The samples were prepared by incubating 27.5 μM of $hIAPP_{1-37}$ with or without 0.225 mg/mL of POPC 100 nm diameter vesicles overnight at room temperature. The aggregated material was precipitated by mild centrifugation and thoroughly rinsed three times, freeze-dried, resuspended in buffers of variyng D_2O content and measured within 1 mm path length Hellma cells, in a rotating sample rack[31] to avoid sedimentation of the aggregates. The D22 instrument was set to measure neutrons scattered over a range of momentum transfer (Q) from 0.008 to 0.5 Å^{-1}. Contrast match experiments were performed by varying the solvent D_2O/H_2O ratio, in order to determine the scattering length density (SLD: see Supporting Information for definition) of the aggregates, which depends on their chemical composition. This technique is precisely explained in a review written by Jacrot in 1976.[32]

Simulated System and Force Field. The insertion potential of mean force (PMF) for a single peptide into a POPC membrane was calculated using replica exchange umbrella sampling (REUS). Three sets of all-atom molecular dynamics (MD) simulations were performed, each with a different IAPP fragment: $hIAPP_{1-20}$, $hIAPP_{23-37}$, or $rIAPP_{1-20}$. The simulated systems consisted of the desired IAPP fragment, 126 POPC molecules, approximately 8800 water molecules, and enough chloride counterions to maintain a zero net charge. The polypeptides and ions were modeled by the AMBER ff99SB*-ILDN force field[33,34] with the TIP3P water model.[35]

The reaction coordinate was defined by the z-component of the distance separating the center-of-mass of the peptide and the POPC bilayer. To initialize the different replicas, the peptide was first inserted into the membrane and equilibrated there. A steered MD simulation was then performed, where the peptide was slowly pulled from the membrane into the water layer over a period of 50 ns while snapshots were stored at different distances. The 12 replicas are distinguished by the equilibrium values of the respective umbrella potentials: $q_{0,i} \in \{0.7$ nm, 1.0 nm, 1.3 nm, ..., 4.0 nm$\}$. In this study, k = 50 kJ mol^{-1} for all replicas. Coordinate exchanges were periodically proposed for adjacent replicas along the reaction coordinate.

For membrane conductance measurements, Neutron-using techniques and simulations, detailed protocols are provided as Supporting Information.

DOI: 10.1021/jacs.6b06985
J. Am. Chem. Soc. 2017, 139, 137−148

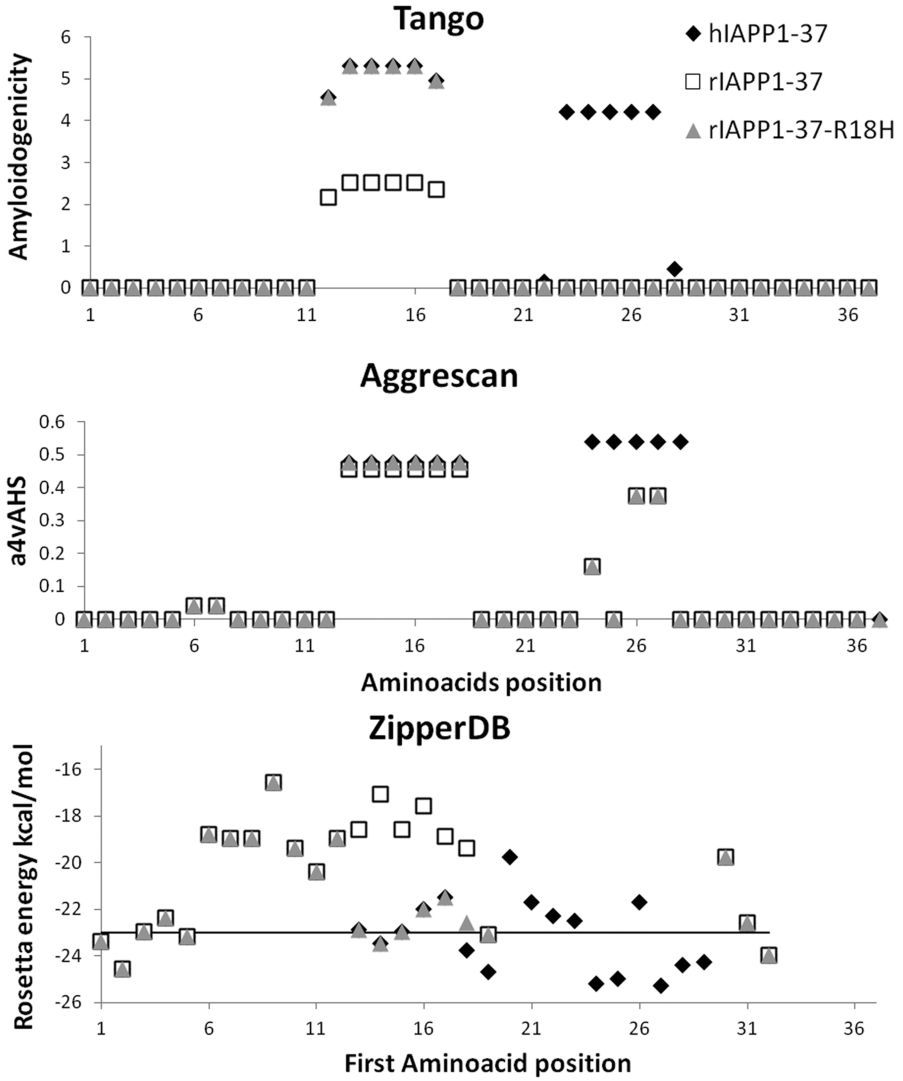

Figure 2. Amyloidogenicity predictions of human (black diamonds), rat (white squares) and chimeric (gray triangles) peptides by three different pieces of software: Tango (Top graph), Aggrescan (middle graph) and ZipperDB (bottom graph). In ZipperDB graph, the continuous black line figures the score below which the peptide can be considered as amyloidogenic.

RESULTS AND DISCUSSION

Amyloidogenicity Prediction and Peptides Characterization in Absence of Lipids. Previous studies of IAPP have shown that several fragments exhibit amyloid aggregation.[36−39] In particular, Green et al.[17] showed that the mutation of arginine 18 to histidine conferred amyloidogenicity to the rat IAPP peptide. The amyloidogenic nature of $hIAPP_{1-37}$, $rIAPP_{1-37}$ and the mutant $rIAPP_{1-37}$R18H was evaluated by three distinct algorithms. The resulting predictions are given in Figure 2. Two hotspots were detected: one in the N-ter (region 12−18), one in the C-ter (region 23−28). According to TANGO and ZIPPER-DB, the amyloid propensity of the N-ter is increased when position 18 is a histidine rather than an arginine. Therefore, due to this single point difference the N-ter hotspot of $hIAPP_{1-37}$ and $rIAPP_{1-37}$R18H has a higher predicted amyloid propensity than that of the wild type $rIAPP_{1-37}$. AGGRESCAN does not detect this difference. The C-ter hotspot was only detected in $hIAPP_{1-37}$ for all three algorithms. This region is predicted to form β-hairpin structures, a feature that has also been observed in our own simulations.[18] Together, these results suggest that the human IAPP contains several hot spots for amyloid aggregation, as seen in previous experimental studies,[36−39] but the C-terminal 20−29 region is primarily responsible for its higher propensity to form amyloid aggregates relative to the rat peptide.[40,41] Although the N-terminal half displays less amyloidogenic behavior, there is experimental evidence for the predicted enhanced amyloid behavior caused by the presence of a histidine in position 18, as in the human variant, rather than an arginine found in the rat variant.[17]

Amyloid peptides and, more generally, aggregation prone biomacromolecules, are well-known to behave nonreproducibly. They are extremely sensitive to parameters that are not typically controlled when handling peptide solutions, such as pressure, shear forces applied by pipetting, or vortexing. Therefore, as a precautionary measure, the peptides were submitted to classical assays in the absence of lipids to ensure that they behave, in our experimental conditions, in the same way as reported in the literature: ThT binding assay, DLS and CD measurements. The results of these measurements are shown in Figures 3 and 4.

The raw autocorrelogram from DLS measurements, as well as the TEM images are shown in the Supporting Information.

DOI: 10.1021/jacs.6b06985
J. Am. Chem. Soc. 2017, 139, 137−148

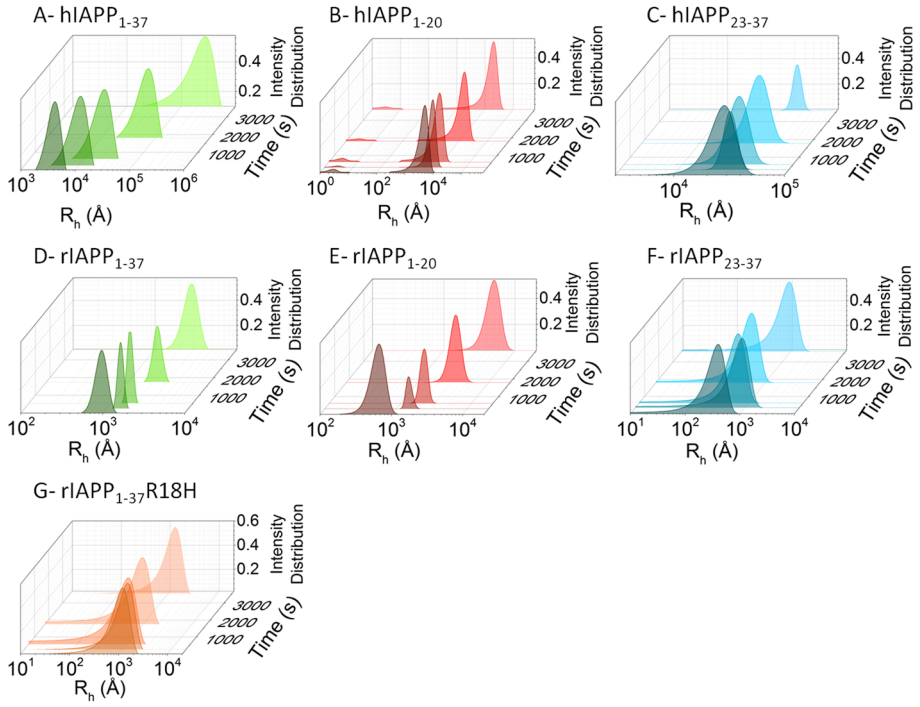

Figure 3. Population distribution extracted from DLS measurement of each peptide within 1 min upon dilution in buffer, and consecutively after 5, 10, 30 and 60 min (darkest to lightest). Peptides are $hIAPP_{1-37}$ (A), $hIAPP_{1-20}$ (B), $hIAPP_{23-37}$ (C), $rIAPP_{1-37}$ (D), $rIAPP_{1-20}$ (E), $rIAPP_{23-37}$ (F) or $rIAPP_{1-37}R18H$ (G). The experiment was repeated twice.

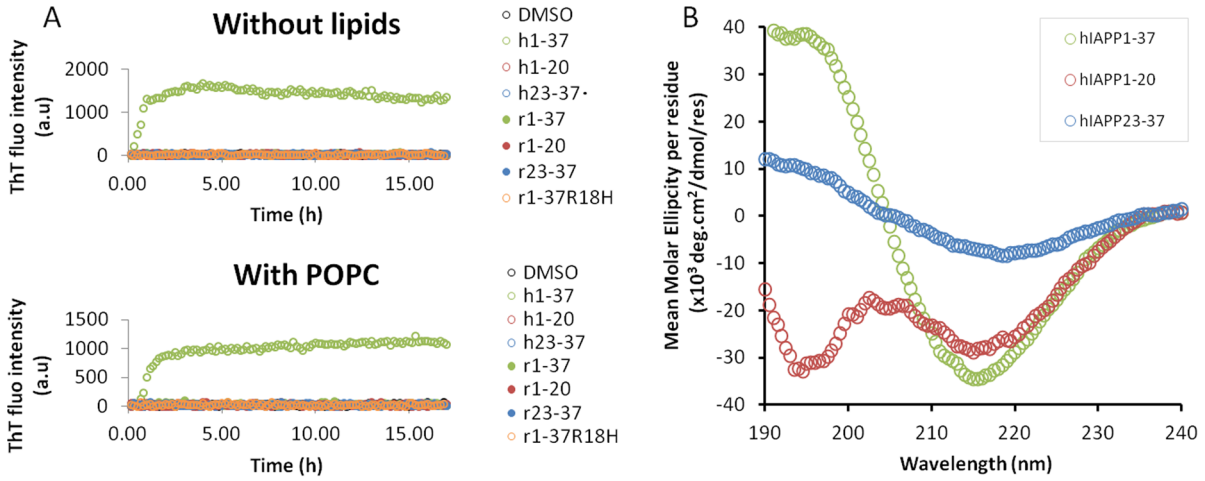

Figure 4. Thioflavin T fluorescence of IAPP fragments and CD spectra of the human peptides. (A) Fluorescence intensity at 490 nm as a function of time. The measurement started concomitantly with the addition, in Thioflavin T-containing buffer, of $hIAPP_{1-37}$ (green open circles), $hIAPP_{1-20}$ (red open circles), $hIAPP_{23-37}$ (blue open circles), $rIAPP_{1-37}$ (green full circles), $rIAPP_{1-20}$ (red full circles), $rIAPP_{23-37}$ (blue full circles) or $rIAPP_{1-37}R18H$ (orange open circles). (B) Circular Dichroism spectra of $hIAPP_{1-37}$ (green), $hIAPP_{1-20}$ (red) and $hIAPP_{23-37}$ (blue) in absence of lipids. The experiments were repeated 2 to 3 times.

Upon diluting the stock solution 50 times in aqueous buffer, $hIAPP_{1-37}$ starts to aggregate into a broad particle distribution in which the hydrodynamic radius (R_H) increases by roughly 2 orders of magnitude over 1 h (from ~500 to 60 000 nm) (Figure 3A). The formation of these aggregates is concomitant with an increase of Thioflavin T fluorescence (Figure 4). The final structure measured by circular dichroism is dominated by antiparallel β-sheet character, which is shown by the ellipticity maximum at 195 nm. However, the displacement of the minimum to 220 nm also suggests the presence of some α-helical character (Figure 4). As confirmed by transmission electron microscopy (TEM), $hIAPP_{1-37}$ forms amyloid fibers, as expected, in presence or absence of lipid vesicles (Supporting Information Figure S1A and G).

The $hIAPP_{1-20}$ fragment forms two distinct populations: a large one made of very small particles with R_H on the order of 1 nm, and a population of small aggregates with size increasing from 500 to 2000 nm with time (Figure 3B). The first population could indeed be monomers or oligomers of very low level that persist over the entire length of the process. These structures do not bind Thioflavin T, and the secondary structures revealed by circular dichroism are a mixture of α-helix and random coil conformations (Figure 4). These observations are in line with previously reported studies.[19,20]

DOI: 10.1021/jacs.6b06985
J. Am. Chem. Soc. 2017, 139, 137−148

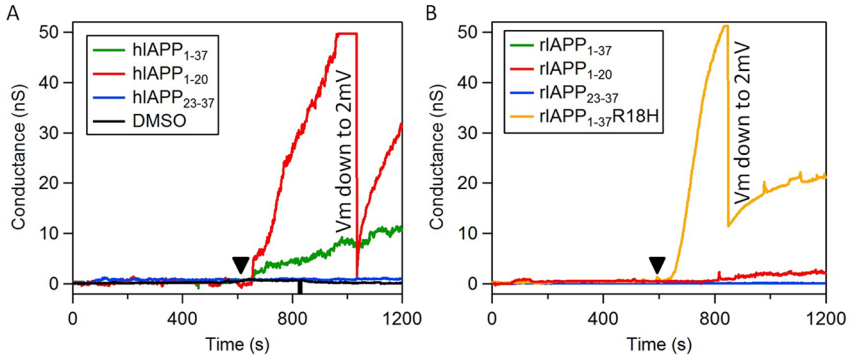

Figure 5. Conductance of a POPC bilayer plotted as a function of time. The black arrow figures the time point of injection of the peptides: full length (green), fragment 1−20 (red) and fragment 23−37 (blue). The left plot (A) contains the human-derived peptides and the right plot (B), the rat-derived peptides, including the chimeric rIAPP$_{1-37}$R18H (orange). When the amplifier saturated, the tension was decreased from 10 mV to 2 mV to continue the measurement. Each data set had been reproduced 3 to 5 times.

Despite the low concentration, TEM enabled us to observe the morphology of these aggregates: some thin and short filaments (Figure S1B).

The hIAPP$_{23-37}$ fragment, thought to constitute the spine of IAPP amyloid fibrils,[21] forms aggregates with a size around 3000 nm (Figure 3C) that does not evolve with time. They are slightly larger than hIAPP$_{1-20}$ aggregates, but much smaller than amyloid fibers formed by hIAPP$_{1-37}$. The circular dichroism measurement shows a minimum of ellipticity between 215 and 220 nm, which is a clear indication of β-sheet structure (Figure 4). Wiltzius et al.[21] showed that both halves of this peptide are able to form amyloid fibrils. The complete peptide hIAPP$_{23-37}$ does not form amyloid fibers but only short and thin filaments, as revealed by TEM (Figure S1C). The absence of ThT fluorescence enhancement (Figure 4) suggests that they are not amyloids. The noticeable feature of this peptide is that the aggregates, although quite large, are already formed at the beginning of the DLS kinetics measurements, less than 1 min after dilution and, therefore, this aggregation is particularly rapid compared to that of hIAPP$_{1-37}$. No intensity correlation could be measured from hIAPP$_{1-37}$ and hIAPP$_{23-37}$ in DMSO, confirming that they remain monomeric in this solvent.

The rat peptides rIAPP$_{1-37}$ and rIAPP$_{1-20}$ show a similar behavior in DLS (Figure 3D and 3E). They both form species of moderate size, even smaller than the hIAPP$_{1-20}$ structures. TEM revealed the presence of some rare amorphous aggregates (Figure S1D and E). However, the C-terminal end, rIAPP$_{23-37}$ peptide, displays a very different behavior. Although the UV absorbance spectrum confirms its presence in the expected concentration, the entities that it forms are much smaller and barely detectable by DLS (Figure S2), suggesting that a large proportion of it remains undetectable and only a small proportion makes small aggregates of about 30 nm R_H. No structure could be observed by TEM. As expected, none of the three rat peptides triggers ThT fluorescence enhancement.

The chimeric peptide rIAPP$_{1-37}$R18H forms clusters of the order of 50 nm R_H, which do not evolve in time. Nor does it form an amyloid structure, as indicated by the absence of ThT fluorescence enhancement. In their report, Green et al.[17] suggested the possibility of rIAPP$_{1-37}$R18H fibril formation, but with a very low nucleation rate. They conducted their assay with a peptide concentration of 200 μM. Our measurements used a much lower concentration of peptide (28 μM) which could explain why we did not detect any fibrillation of rIAPP$_{1-37}$R18H. Although the DLS results indicates that they exist, we could not observe rIAPP$_{1-37}$R18H aggregates in absence of lipids by TEM, probably due to their low concentration. However, in the presence of POPC vesicles, short and straight filaments were visible (Figure S1H). In agreement with the results of Green et al.,[17] we could not detect any ThT fluorescence enhancement.

To summarize, the DLS results (Figure 3 and S2) show that both hIAPP$_{1-20}$ and rIAPP$_{1-20}$ form aggregates of moderate size, in agreement with the predictions of an aggregation hotspot in the 12−18 amino acids region (Figure 2) but a large proportion of hIAPP$_{1-20}$ constitutes a subnanometric particle population. Aggregates of the two peptides show different morphologies, underlying the role of Histidine 18 in the fibrillation process (Figure S1B and E). Another difference between the rat and the human IAPP derives from the behavior of the 23−37 fragments, where most of the sequence differences are located. The human hIAPP$_{23-37}$ rapidly forms short filaments while the rat rIAPP$_{23-37}$ keeps monomeric (and undetectable) or forms rare small oligomers. And the chimeric peptide rIAPP$_{1-37}$R18H rapidly aggregates into small structures, possibly short filaments. These results suggest that both the 1−20 part of the human peptide and the 23−37 part are prone to self-assembly separately, but the presence of both segments is necessary to observe a very long-range aggregation, shown only by hIAPP$_{1-37}$, and corresponding to amyloid fibers, in their strict definition.

Lipid Bilayer Permeation. The ability of the seven peptides to permeate lipid bilayers was assessed by electrophysiological measurements with POPC bilayers built at the interface of two droplets. Figure 5 illustrates the changes in conductance triggered by the human (A) and rat (B) peptides.

Injection of the full length hIAPP$_{1-37}$ peptide leads to an increase of the bilayer conductance with a rate of 0.02 nS/s whereas, as expected,[17] the rat homologue has no effect on membrane permeability. The human C-terminal fragment hIAPP$_{23-37}$, as well as the rat fragments rIAPP$_{1-20}$ and rIAPP$_{23-37}$, does not modify the conductance of the bilayer. However, injection of the human N-terminal fragment hIAPP$_{1-20}$ triggers a large increase in current at a rate of about 0.17 nS/s. Similarly, the injection of the chimeric peptide rIAPP$_{1-37}$R18H causes a large increase in permeability at a rate of 0.25 nS/s. According to these electrophysiologic measurements, hIAPP$_{1-20}$ shows a high capacity to permeate POPC bilayers, higher than that of the full-length hIAPP$_{1-37}$. These

DOI: 10.1021/jacs.6b06985
J. Am. Chem. Soc. 2017, 139, 137−148

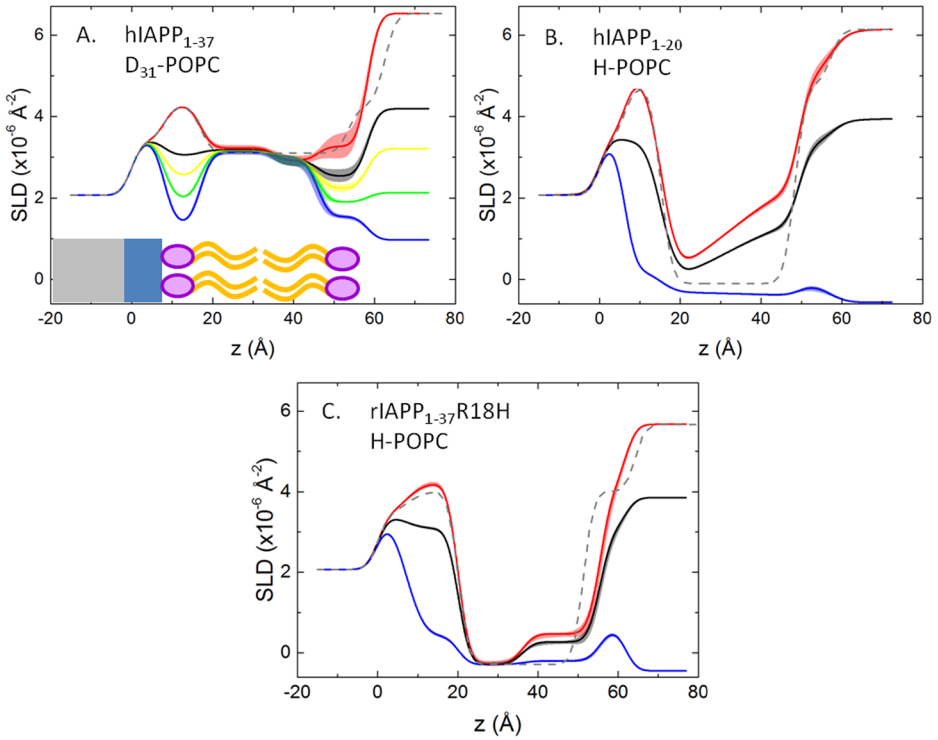

Figure 6. SLD profiles obtained from fits of the NR curves recorded after peptide injection, at different contrasts: 0% D_2O in blue, 38% D_2O in green, 52% D_2O in yellow, 66% D_2O in black, 100% D_2O in red. For comparison purposes the SLD curves of the pristine lipid bilayers before peptide injection in 100% D_2O buffer are also shown as a gray dotted line. The sketch inserted in graph A enables to locate each component along the *z*-axis. It shows the silicon crystal (gray) and its oxidation layer (blue) and the two lipid leaflets with the headgroups (purple) and aliphatic chains (orange). Confidence intervals for the SLD curves are plotted as line thickening. These measurements have been repeated twice.

results are in qualitative agreement with those of Brender et al.[19] However, Khemtemourian et al.[42] and Heyl et al.[43] reported that $hIAPP_{1-37}$ was more efficient for membrane permeation than $hIAPP_{1-19}$. This discrepancy cannot be explained by the electrostatic properties of the bilayer, and remains to be clarified. Taken together, these results confirm that the membrane disturbance by a peptide is not a direct consequence of its amyloid aggregation. If this in vitro permeation assay is accepted as a model of in vivo cytotoxicity, our results strengthen the conclusion of Brender et al.[19] that amyloidogenicity and cytotoxicity are induced by two different regions of the peptide sequence. In vivo, lipid charge and length[15,42,44−46] as well as the presence of cholesterol[47] and probably other components may be necessary to explain the cellular selectivity of IAPP cytotoxicity.

Structural Investigation. The structure of the bilayer in the direction normal to its surface was characterized using neutron reflectometry before and after the introduction of peptides in its vicinity. The scattering length density (SLD) profiles resulting from the analysis of the collected reflectivity curves are presented in Figure 6.

Comparison of the SLD profiles, which are directly related to the structure and composition of the bilayer, indicates that bilayer structure remains unperturbed by the injection of any of the rat variants $rIAPP_{1-37}$, $rIAPP_{1-20}$, $rIAPP_{23-37}$ or the human C-terminal end $hIAPP_{23-37}$ (data not shown). Introduction of $hIAPP_{1-37}$, $hIAPP_{1-20}$ or $rIAPP_{1-37}$R18H perturbs the structure of the bilayer to different extents (Figure 6). In all three cases, only the leaflet of the bilayer directly in contact with the buffer solution is disturbed.

The most intriguing effect was observed in the presence of the $hIAPP_{1-20}$ peptide (Figure 6B) where the SLD of the outer leaflet changed drastically. This change in the lipid SLD profile was found to be correlated linearly with the buffer SLD, suggesting that a large portion of the lipid molecules initially present in the leaflet was removed and replaced by buffer molecules. Furthermore, SLD profiles show a gradual interface between the inner and outer leaflets, rather than a clear step. This is indicative of a strong bilayer destabilization and a blurred boundary between these leaflets. Simply removing lipids of the first leaflet would result in exposing the aliphatic chains of the second leaflet to solvent, which is very unfavorable. We propose the following two scenarios:

- The $hIAPP_{1-20}$, known to form an amphiphilic helix,[48] covers the interface generated by lipid depletion. A large hydration level of the peptide could account for its contribution to the bilayer composition not being detected.
- The lipids rearrange in a bilayer of lower density, which could explain the loose boundary between the two leaflets. $hIAPP_{1-20}$ would return to solution complexed with lipid molecules, as suggested by a past NMR study.[49] This hypothesis is better supported by our results. The degree of oligomerization of the peptide when it leaves the membrane cannot be determined by this experiment.

In the presence of $hIAPP_{1-37}$ (Figure 6A) the SLD of the outer leaflet decreased for all solvent contrast conditions. Such an effect could be attributed to the insertion of the peptide, mainly among the headgroups of the lipids, the aliphatic chains

DOI: 10.1021/jacs.6b06985
J. Am. Chem. Soc. 2017, 139, 137−148

being only slightly disturbed. No insertion of solvent across the bilayer was observed in this case.

In the presence of rIAPP$_{1-37}$R18H (Figure 6C), the SLD of the accessible leaflet is also perturbed, indicating the insertion of a small amount of peptide and solvent. This perturbation is weak compared to the effect of hIAPP$_{1-20}$ (Figure 6B), although both peptides caused similar dramatic increases in membrane ionic conductance.

Together with the membrane permeation measurements, these results can be explained in the following way: Upon the interaction of hIAPP$_{1-20}$ with the bilayer, lipids are extracted from the bilayer; hIAPP$_{1-20}$ itself leaves the bilayer and the two leaflets are forced to rearrange into a less dense, and therefore more permeable structure.

The hIAPP$_{1-37}$ fragment also interacts with the bilayer, but its C-terminus half keeps it mainly at the surface, among the headgroups of the lipids. The C-terminus half is probably involved in amyloid aggregates, which could prevent a deeper insertion due to steric exclusion. Whereas for rIAPP$_{1-37}$R18H, whose C-terminus end is not amyloidogenic, the peptide spreads equally between the headgroups and the aliphatic chain region of the leaflet. It also leads to depletion of lipids and their replacement with solvent molecules.

The disturbance of only one leaflet of the bilayer may be the result of an experimental artifact caused by the strong interaction between the silicon-oxide surface and the lipid headgroups of the upper bilayer leaflet. Nevertheless, only one leaflet was disrupted in similar experiments carried out with a tethered bilayer[50] in the presence of α-synuclein. Whether the effect is on one or on both leaflets of the bilayer, the lipid depletion is consistent with the thinning of the bilayer observed in other studies,[13,51] and could be a mechanism of membrane permeation.

These interfacial results raise questions concerning the fate of the removed lipids. In order to address this, we took advantage of the unique capability of neutrons to distinguish between biomolecules associated in complexes suspended in solution.[32] SANS measurements were performed to study the composition of hIAPP$_{1-37}$ aggregates formed in the presence or absence of POPC by exploiting the contrast variation technique.

Figure 7 presents the results of these measurements in terms of the square root of the averaged coherent scattering intensity measured at small angle (I_{SA}, $0.008 < Q < 0.015$ Å^{-1}), normalized by the mass concentration of the aggregates, which linearly depends on the buffer D_2O content. The aggregates formed in the presence of POPC are bigger than the aggregates formed in its absence, as shown by the slope of their contrast match point. From the linear fits of each contrast series (dotted lines), the match point of the aggregates, i.e. the D_2O content at which the aggregates and the buffer have the same SLD, was calculated to be only 31% D_2O for hIAPP$_{1-37}$ aggregated in the presence of POPC vesicles versus 39% of D_2O for hIAPP$_{1-37}$ aggregated in the absence of lipids, which is a reasonable value for the peptidic material. The SLD of POPC alone, which has no exchangeable hydrogen and a specific volume of 1246 Å^3,[52] was calculated to be 0.27×10^{10} cm^{-2}, and therefore, would match the SLD of a 12% D_2O buffer. Therefore, one can estimate that the aggregates are constituted of 70% peptide and 30% lipids. These volume fractions correspond to about 1.6 lipid molecules per peptide, considering a volume of 4726 Å^3 for the peptide.[53] Therefore, the lipids extracted from the bilayer coaggregate with peptide into amyloids structures.

Mechanistic Explanation. A subset of the peptides considered in our experiments was also examined in simulations, namely hIAPP$_{1-20}$, rIAPP$_{1-20}$, and hIAPP$_{23-37}$. As mentioned above, we eliminate the role that aggregation may play by focusing on a single peptide, which allows one to develop a clearer and more tractable picture of how the N- and C-terminus of hIAPP may interact with the membrane. For each peptide, the location of the free energy minimum was calculated as a function of its depth in the bilayer, measured as the z-component of the distance between the center-of-mass of the peptide and that of the lipids. A distance of 0.0 nm corresponds to the center of the bilayer, where the leaflets meet. For reference, in our simulations, POPC headgroups are located about 1.5−2.0 nm from the interface between the two leaflets. The potentials of mean force (PMFs) for insertion, calculated from REUS simulations,[54,55] are depicted in Figure 8. The potential at a distance of 4.0 nm is defined to be zero.

The PMFs of hIAPP$_{1-20}$, rIAPP$_{1-20}$, and hIAPP$_{23-37}$ all exhibit global minima at distances that require some degree of association with the POPC bilayer. In all three cases, the PMF slopes upward and flattens from 3.0 to 4.0 nm, at which point the peptide and lipids are dissociated. The PMF of hIAPP$_{1-20}$

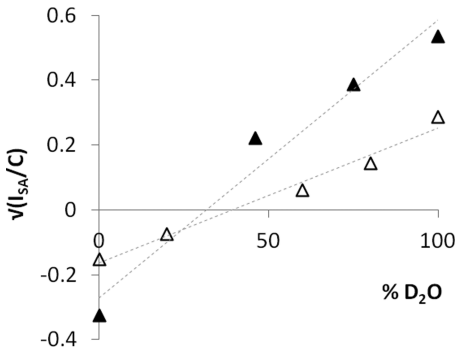

Figure 7. Contrast match point from SANS measurements of hIAPP$_{1-37}$ aggregates formed in absence (open triangles) or presence (black triangles) of POPC. The square root of the neutron coherent scattering intensity averaged over the Q-range of 0.008 to 0.015 Å^{-1} and normalized by the sample mass concentration ($\sqrt{(I_{SA}/C)}$), is plotted as a function of the D_2O content of the solvent. The results are from one single experiment.

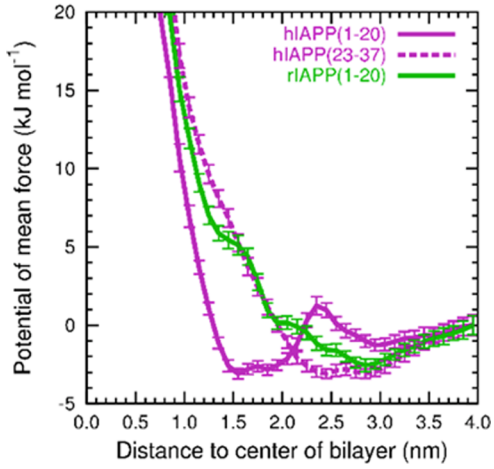

Figure 8. Potentials of mean force as a function of the z-component of the distance between the center-of-mass of the peptide and that of the POPC bilayer.

DOI: 10.1021/jacs.6b06985
J. Am. Chem. Soc. 2017, 139, 137−148

has a global minimum of −3.1 kJ mol^{-1} at 1.6 nm, which is just beneath the lipid headgroups and among the hydrophobic tails. States from 1.5 to 2.0 nm are within 1.0 kJ mol^{-1} of the global minimum, implying only a weak preference for the base of the headgroups with respect to the middle or top. The PMF rises steeply as the peptide inserts deeper. There is also a free energy barrier to insertion into the headgroups, peaked at 2.4 nm. In other words, the insertion of hIAPP$_{1-20}$ is an activated process requiring that an energetic barrier be overcome to reach the global minimum.

The free energy profile for hIAPP$_{23-37}$ exhibits two global minima of essentially equal stability, at 2.4 and 2.8 nm. Both have a magnitude of −3.1 kJ mol^{-1}. As mentioned earlier, the rat peptide segment rIAPP$_{1-20}$ only differs from hIAPP$_{1-20}$ by residue 18, and it has a global minimum near 2.9 nm of −2.6 kJ mol^{-1}. At those distances, some (but not all) residues interact with the headgroups. Neither hIAPP$_{23-37}$ nor rIAPP$_{1-20}$ exhibit any metastable states among the headgroups or the lipid tails. In summary, these simulations show that the energetic landscape of the hIAPP$_{1-20}$ fragment favors interaction with the amphiphilic region situated at the base of lipid headgroups, while the two other peptides, hIAPP$_{23-37}$ and rIAPP$_{1-20}$ do not show this specificity. This particular behavior has to be correlated with the high impact of hIAPP$_{1-20}$ on the bilayer, measured by electrophysiology and neutron reflectometry. It has to be mentioned that all the global minima are characterized by an energy very close to k_BT. This implies that peptides will only fleetingly occupy these positions and that experimental observation of bound states is unlikely, in agreement with our NR results showing that the bilayers were not covered by a peptide layer. This low affinity also implies that once a peptide inserts into the membrane, its proximity with lipid molecules may promote the creation of a peptide-lipid bound state, that could result in the lipid depletion effect observed experimentally. Previous works have shown that the association and insertion of the full hIAPP peptide are mediated by the N-terminus.[56,57] Note that the removal of lipids from the bilayer would not be observed in the current simulation setup due to the long time scales that would be required for such a dissociation. Furthermore, the size of the simulation box would preclude a complete dissociation from occurring; the hole left by the departing lipids would be a larger portion of the membrane in the simulation and the time scales required for a lipid to change leaflets to correct for such a dissociation are much larger than what is practically possible to simulate. The change of residue 18 from histidine in hIAPP$_{1-20}$ to arginine in rIAPP$_{1-20}$ causes a substantial change of the PMF. The guanidinium side chain of arginine is bulkier and more hydrophilic than the imidazole side chain of histidine, and arginine carries a positive charge at neutral pH, while histidine does not. These properties may impede the insertion of Arg18 into the membrane.

In Figure 9, we plot the abundance of helical and strand-like secondary structures for each residue as a function of distance from the center of the bilayer.

In bulk solution, all three fragments exhibit some secondary structure, in agreement with previously described CD spectra (Figure 4B). The hIAPP$_{1-20}$ fragment has some helix from Ala8 to Val17 and occasional antiparallel β-sheet, with Cys2−Asn3 on one strand and Leu16−Val17 on the other. The hIAPP$_{23-37}$ fragment contains non-negligible quantities of both helix and β-strand character in solution. The β-sheet signal for hIAPP$_{23-37}$ is weaker than would be expected from the above CD spectra;

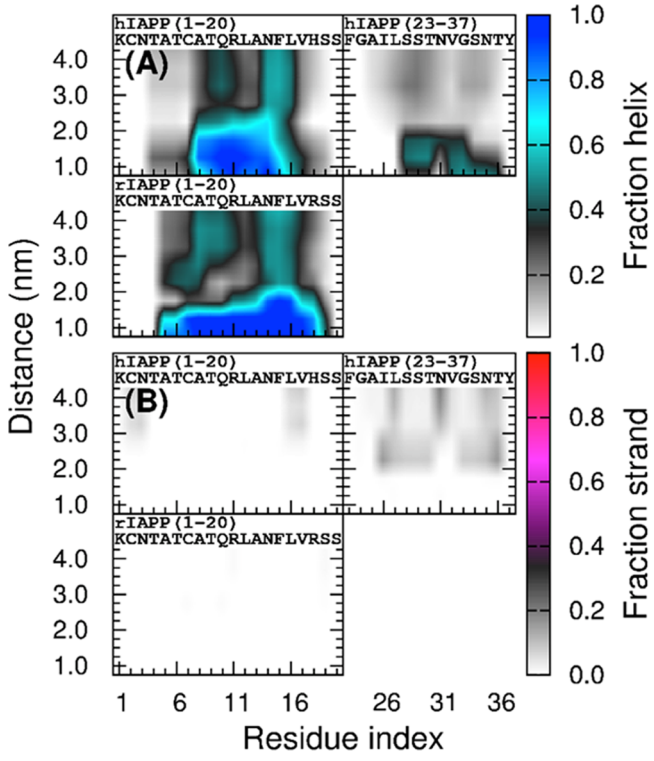

Figure 9. Fractional secondary structure as a function of residue and of z-distance between the center-of-mass of the peptide and that of the POPC bilayer. Secondary structure is assigned by the DSSP algorithm. Statistics are based on all production snapshots in all replicas. The fractional secondary structure for a particular residue at a particular distance is based on the number of snapshots corresponding to that distance. (A) The fraction of helix for a particular residue is defined as the fraction of those snapshots in which the residue is assigned a helix-like secondary structure by DSSP (i.e., α-helix, 310-helix, or π-helix). (B) The fraction of strand is defined as the fraction of those snapshots in which the residue is assigned a strand-like secondary structure by DSSP (i.e., β-sheet or β-bridge).

this is possibly due to the fact that simulations only consider a single peptide, and the β-sheets formed above are intermolecular in nature. The rIAPP$_{1-20}$ fragment has a stronger propensity for helical structure from Cys7 to Arg11, but appears to be devoid of β-strand. This is not unexpected, because an antiparallel β-sheet between Cys2−Asn3 and Leu16−Val17, as in hIAPP$_{1-20}$, would place Lys1 and Arg18 in close proximity. Electrostatic repulsion and steric considerations render such a conformation energetically unfavorable. This is in agreement with the experimental predictions presented above.

As mentioned earlier, a simple sequence comparison of hIAPP$_{1-20}$ and rIAPP$_{1-20}$ indicates that the mutation of His18 in hIAPP to Arg18 in rIAPP is ultimately responsible for the difference in the equilibrium insertion depth between the two fragments. The increased bulk and hydrophilicity of arginine provides a rationale for its reluctance to immerse in the lipid tails. Miller et al.[58] reported that the free energy of transfer of histidine from the protein surface to the interior is 0.08 kJ mol^{-1}, and the free energy of transfer of arginine is 5.86 kJ mol^{-1}. Since the protein interior typically consists of hydrophobic residues, this metric is a reasonable estimate of the transfer free energy from bulk water to a hydrophobic fluid (such as the center of a lipid bilayer). If we set to zero the free energy of both histidine and arginine in water, then to insert

DOI: 10.1021/jacs.6b06985
J. Am. Chem. Soc. 2017, 139, 137−148

arginine into the lipid tails requires 5.77 kJ mol^{-1} more work than to insert histidine. We plot radial distribution functions (Figure S5) of the atoms of residue 18 (histidine or arginine) with respect to the POPC headgroups at the respective free energy minima identified in Figure 8. The distinguishing feature between the profiles of His18 and Arg18 is a peak at 0.2 nm for Arg18 not present for His18. This peak corresponds to hydrogen bonds between the guanidinium side-chain of Arg18 with the phospho groups of POPC.

CONCLUSION

Our initial biophysical characterization shows that in the absence of lipids, $hIAPP_{1-37}$ forms large amyloid aggregates in buffer solution. The carboxy-terminus half of the peptide, $hIAPP_{23-37,}$ rapidly forms aggregates that are rich in β-sheet but do not bind ThT, and $rIAPP_{23-37}$ remains monomeric. Concerning the 1−20 region, both human and rat fragments form aggregates of moderate size, the human ones being slightly bigger and filamentous. The rat peptide and the chimeric $rIAPP_{1-37}$R18H peptide also form aggregates of moderate size. Therefore, all peptides but $rIAPP_{23-37}$ show propensity to self-assemble but the presence of both aggregation hotspots of hIAPP1−37 seem necessary to form long amyloid fibers.

Our results from electrophysiological recordings and neutron reflectometry show that $hIAPP_{1-20}$, either alone or associated with a nonamyloidogenic C-terminal part ($rIAPP_{1-37}$R18H), disrupts a POPC bilayer both in its role as an ionic barrier and its structure. The difference between $hIAPP_{1-20}$ and $rIAPP_{1-20}$ is striking considering their sequence similarity: $hIAPP_{1-20}$ dramatically increases membrane permeation while $rIAPP_{1-20}$ has almost no effect. Their single difference, the amino acid in position 18 being a histidine or an arginine, therefore plays a crucial role by modulating the insertion depth of the fragments and the energy barrier for insertion, as shown by our simulations. Indeed, the exchange of histidine 18 for an arginine would weaken the interactions with the base of lipid headgroups and increase the amount of work necessary to insert the peptide into the bilayer.

The association of this very membrane-reactive $hIAPP_{1-20}$ with an amyloidogenic C-terminal half (to form $hIAPP_{1-37}$) partially inhibits its effect, probably by promoting aggregation into structures that are unable to affect the membrane, while the C-terminal part on its own ($hIAPP_{23-37}$) has neither a structural nor a functional impact on the bilayer.

Neutron reflectometry shows that the membrane disturbance by $hIAPP_{1-20}$ is correlated with a major depletion of lipids, while SANS reveals that about 1 to 2 lipids per peptide are sequestered within the $hIAPP_{1-37}$ amyloid aggregates formed in the presence of POPC vesicles.

Together, these results suggest a cytotoxic mechanism for $hIAPP_{1-37}$ that we have illustrated in Figure 10. Such a mechanism would proceed in parallel and independently of the amyloid aggregation, as proposed by Glabe in 2010.[2] Some IAPP peptides released in proximity of a lipid bilayer would interact with it, either in a monomeric form or already assembled in oligomers, due to the 1−20 region and its particular affinity for the base of the lipid headgroups. Indeed, DLS shows that the most membrane-active peptide, $hIAPP_{1-20}$, exhibits a large population of persisting subnanometric particles when diluted in buffer. This lipid extraction, already observed by Sparr et al.[59] and more recently by Junghans et al.,[60] is indeed substantial and sufficient to explain at least part of the

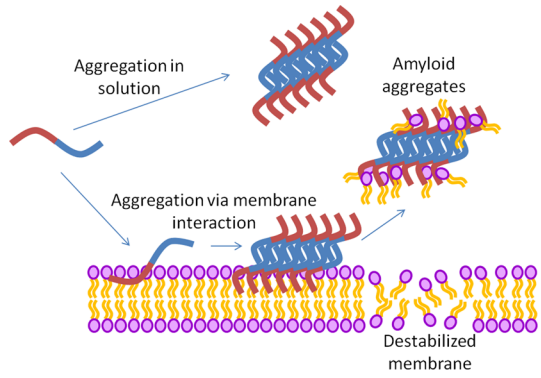

Figure 10. Model of independent processes of aggregation and membrane interaction of human IAPP, operating together to membrane permeation and cytotoxic properties. Note that the initial entity is not necessarily a monomer.

membrane permeation and cytotoxicity. In parallel, the amyloid aggregation ensues, triggered by the 23−37 region prone to hydrophobic interaction. It includes the self-assembly of peptides or oligomers while they stand in solution and in the bilayer, and are associated or not with lipids, competing partially with the permeation mechanism. The presence of a histidine at position 18, as opposed to an arginine, enhances the cytotoxic process by raising the affinity of the peptide for the base of lipid headgroups while ensuring a relatively low energetic cost of insertion into the bilayer.

This model is compatible with previous literature reports.[61] In particular, it accounts for observed peptide insertion into the lipid bilayer and membrane thinning.[13] The hypothesis that lipid depletion is the mechanism by which amyloid peptides disrupt the membrane has gained more support over the past few years[59,62−66] for various amyloid peptides. Our observations do not exclude totally the coexistence of transient pores through the lipid bilayer formed by IAPP. Such an interaction may have been disfavored in our neutron reflectometry experimental setup due to the strength of interaction between the silicon crystal and the lipid headgroups. However, such species, crossing the whole thickness of the bilayer, were not observed here, although they were initially expected.

The hypothesis of oligomers (not necessarily pores) being the cytotoxic species of amyloids is largely supported and used by scientists to interpret their data, although their precise structure remains difficult to characterize. Our experiments give no precise information about the oligomeric state of the peptide when it interacts with the membrane and leaves it together with some lipids attached. However, the two findings: the existence of a membrane-disturbing oligomer and the phenomenon of lipid extraction, are perfectly compatible within the scenario that we propose.

The observation that amyloid aggregation and membrane perturbation are two independent processes running in parallel raises questions about the link between the pathological loss of cells and the presence of amyloid aggregates in key organs. Amyloidogenicity could be a defense mechanism selected through evolution to silence cytotoxic peptides and delay the onset of diseases to an age where reproduction is no longer affected. Several amyloidoses are indeed related to aging. However, this is largely beyond the scope of this publication and would require further investigation, including a phylogenetic study of when the differentiating mutations between the rat and the human peptides occurred, as well as epidemiological

DOI: 10.1021/jacs.6b06985
J. Am. Chem. Soc. 2017, 139, 137−148

and clinical genetic studies. To further our understanding, we plan to focus on similar studies of other amyloid peptides as well as more biologically relevant membranes in order to shed light on the common and specific modalities of each of them.

■ ASSOCIATED CONTENT

Supporting Information

The Supporting Information is available free of charge on the ACS Publications website at DOI: 10.1021/jacs.6b06985.

Transmission electron microscopy; dynamic light scattering; membrane conductance measurement; neutron reflectometry; small angle neutron scattering; molecular dynamics simulations (PDF)

■ AUTHOR INFORMATION

Corresponding Author

*martela@ill.fr

ORCID

Anne Martel: 0000-0002-1232-8519

Yuri Gerelli: 0000-0001-5655-8298

Juan J. de Pablo: 0000-0002-3526-516X

Notes

The authors declare no competing financial interest.

■ ACKNOWLEDGMENTS

Authors are very thankful to David Eisenberg (UCLA, USA) and Jacques-Philippe Colletier (IBS, Grenoble, FRANCE) for the gift of peptide fragments that enabled us to start this study, to M. Jamin, J. Perard and C. Mas for their training and the availability of the Biophysical Platform within the Partnership for Structural Biology and the Grenoble Instruct center (ISBG; UMS 3518 CNRS-CEA-UGA-EMBL) supported by ANR through FRISBI (ANR-10-INSB-05-02) and GRAL (ANR-10-LABX-49-01) projects, to B. Cross, C. Picard (Grenoble-INP, France) and J. Revilloud (IBS, France) for the training in electrophysiology. They also thank Patrick Harrison and Veronica Lattanzi for their participation to the neutron reflectometry experiments. The experimental part of this work has been carried out at the Institute of Structural Biology and the Institut Laue Langevin (instruments D17, D22 and Figaro, chemistry laboratory and Partnership for Soft Condensed Matter) in Grenoble. The Nanosciences Foundation participated to the funding of this work through the Nanobiodrop project. The TEM has been carried out by D. Fenel and G. Schoehn on the platform of the Grenoble Instruct Center (ISBG: UMS 3518 CNRS-CEA-UJF-EMBL) with support from FRISBI (ANR-10-INSB-05-02) and GRAL (ANR-10-LABX-49-01) within the Grenoble Partnership for Structural Biology (PSB). The electron microscope facility is supported by the Rhône-Alpes Region, the Fondation Recherche Medicale (FRM), the fonds FEDER, the Centre National de la Recherche Scientifique (CNRS), the CEA, the University of Grenoble, EMBL, and the GIS-Infrastrutures en Biologie Sante et Agronomie (IBISA). J.J.d.P. is grateful for helpful discussions with J.L. Barrat and financial support that enabled extended stays at the Joseph Fourier University in Grenoble. The contributions of J.J.d.P., A.F., K.H., and L.A. are supported by the National Science Foundation through grant NSF-CBET-1264021. The simulation methods presented here were developed with support from NIST through the Center for Hierarchical Materials Design (CHiMaD).

■ REFERENCES

(1) Ferreira, S. T.; Vieira, M. N. N.; De Felice, F. G. *IUBMB Life* **2007**, *59* (4−5), 332−345.

(2) Glabe, C. *Biophys. J.* **2010**, *98* (3), 3A−3A.

(3) Janson, J.; Ashley, R. H.; Harrison, D.; McIntyre, S.; Butler, P. C. *Diabetes* **1999**, *48* (3), 491−498.

(4) Sipe, J. D.; Cohen, A. S. *J. Struct. Biol.* **2000**, *130* (2−3), 88−98.

(5) Ritzel, R. A.; Meier, J. J.; Lin, C. Y.; Veldhuis, J. D.; Butler, P. C. *Diabetes* **2007**, *56* (1), 65−71.

(6) Meier, J. J.; Kayed, R.; Lin, C. Y.; Gurlo, T.; Haataja, L.; Jayasinghe, S.; Langen, R.; Glabe, C. G.; Butler, P. C. *Am. J. Physiol-Endoc M* **2006**, *291* (6), E1317−E1324.

(7) Milanesi, L.; Sheynis, T.; Xue, W. F.; Orlova, E. V.; Hellewell, A. L.; Jelinek, R.; Hewitt, E. W.; Radford, S. E.; Saibil, H. R. *Proc. Natl. Acad. Sci. U. S. A.* **2012**, *109* (50), 20455−20460.

(8) Fernandez, M. S. *Cell Calcium* **2014**, *56* (5), 416−427.

(9) Quist, A.; Doudevski, L.; Lin, H.; Azimova, R.; Ng, D.; Frangione, B.; Kagan, B.; Ghiso, J.; Lal, R. *Proc. Natl. Acad. Sci. U. S. A.* **2005**, *102* (30), 10427−10432.

(10) Jeworrek, C.; Hollmann, O.; Steitz, R.; Winter, R.; Czeslik, C. *Biophys. J.* **2009**, *96* (3), 1115−1123.

(11) Lorenzo, A.; Razzaboni, B.; Weir, G. C.; Yankner, B. A. *Nature* **1994**, *368* (6473), 756−760.

(12) Cao, P.; Marek, P.; Noor, H.; Patsalo, V.; Tu, L. H.; Wang, H.; Abedini, A.; Raleigh, D. P. *FEBS Lett.* **2013**, *587* (8), 1106−1118.

(13) Relini, A.; Cavalleri, O.; Rolandi, R.; Gliozzi, A. *Chem. Phys. Lipids* **2009**, *158* (1), 1−9.

(14) Last, N. B.; Rhoades, E.; Miranker, A. D. *Proc. Natl. Acad. Sci. U. S. A.* **2011**, *108* (23), 9460−9465.

(15) Lee, C. C.; Sun, Y.; Huang, H. W. *Biophys. J.* **2012**, *102* (5), 1059−1068.

(16) Brender, J. R.; Salamekh, S.; Ramamoorthy, A. *Acc. Chem. Res.* **2012**, *45* (3), 454−462.

(17) Green, J.; Goldsbury, C.; Min, T.; Sunderji, S.; Frey, P.; Kistler, J.; Cooper, G.; Aebi, U. *J. Mol. Biol.* **2003**, *326* (4), 1147−1156.

(18) Chiu, C. C.; Singh, S.; de Pablo, J. J. *Biophys. J.* **2013**, *105* (5), 1227−35.

(19) Brender, J. R.; Lee, E. L.; Cavitt, M. A.; Gafni, A.; Steel, D. G.; Ramamoorthy, A. *J. Am. Chem. Soc.* **2008**, *130* (20), 6424−6429.

(20) Guo, C.; Cote, S.; Mousseau, N.; Wei, G. H. *J. Phys. Chem. B* **2015**, *119* (8), 3366−3376.

(21) Wiltzius, J. J. W.; Sievers, S. A.; Sawaya, M. R.; Cascio, D.; Popov, D.; Riekel, C.; Eisenberg, D. *Protein Sci.* **2008**, *17* (9), 1467−1474.

(22) Fernandez-Escamilla, A. M.; Rousseau, F.; Schymkowitz, J.; Serrano, L. *Nat. Biotechnol.* **2004**, *22* (10), 1302−1306.

(23) Conchillo-Sole, O.; de Groot, N. S.; Aviles, F. X.; Vendrell, J.; Daura, X.; Ventura, S. *BMC Bioinf.* **2007**, *8* (65), 65.

(24) Thompson, M. J.; Sievers, S. A.; Karanicolas, J.; Ivanova, M. I.; Baker, D.; Eisenberg, D. *Proc. Natl. Acad. Sci. U. S. A.* **2006**, *103* (11), 4074−4078.

(25) Tavagnacco, L.; Gerelli, Y.; Cesaro, A.; Brady, J. W. *J. Phys. Chem. B* **2016**, *120* (37), 9987−9996.

(26) Greenfield, N. J. *Nat. Protoc* **2006**, *1* (6), 2876−2890.

(27) Syeda, R.; Santos, J. S.; Montal, M. *J. Biol. Chem.* **2014**, *289* (7), 4233−4243.

(28) Bayley, H.; Cronin, B.; Heron, A.; Holden, M. A.; Hwang, W. L.; Syeda, R.; Thompson, J.; Wallace, M. *Mol. BioSyst.* **2008**, *4* (12), 1191−1208.

(29) Campbell, R. A.; Wacklin, H. P.; Sutton, I.; Cubitt, R.; Fragneto, G. *Eur. Phys. J. Plus* **2011**, *126* (11), 107.

(30) Gerelli, Y. *J. Appl. Crystallogr.* **2016**, *49*, 330−339.

(31) Schweins, R.; Lindner, P.; Bowyer, D.; Amrouni, C.; Nawroth, T. Recent Developments in Sample Environment for SANS at D11@ ILL. In *German Neutron Scattering Conference*; Brueckel, T., Ed.; Forschungszentrum Juelich: Juelich, 2012; p 59.

(32) Jacrot, B. *Rep. Prog. Phys.* **1976**, *39* (10), 911−953.

(33) Lindorff-Larsen, K.; Maragakis, P.; Piana, S.; Eastwood, M. P.; Dror, R. O.; Shaw, D. E. *PLoS One* **2012**, *7* (2), e32131.

(34) Piana, S.; Lindorff-Larsen, K.; Shaw, D. E. *Proc. Natl. Acad. Sci. U. S. A.* **2012**, *109* (44), 17845−17850.
(35) Jorgensen, W. L.; Chandrasekhar, J.; Madura, J. D.; Impey, R. W.; Klein, M. L. *J. Chem. Phys.* **1983**, *79* (2), 926−935.
(36) Gilead, S.; Gazit, E. *Exp. Diabetes Res.* **2008**, *2008*, 256954.
(37) Louros, N. N.; Tsiolaki, P. L.; Zompra, A. A.; Pappa, E. V.; Magafa, V.; Pairas, G.; Cordopatis, P.; Cheimonidou, C.; Trougakos, I. P.; Iconomidou, V. A.; Hamodrakas, S. J. *Biopolymers* **2015**, *104* (3), 196−205.
(38) Ahmed, A. B.; Kajava, A. V. *FEBS Lett.* **2013**, *587* (8), 1089−1095.
(39) Jaikaran, E. T. A. S.; Higham, C. E.; Serpell, L. C.; Zurdo, J.; Gross, M.; Clark, A.; Fraser, P. E. *J. Mol. Biol.* **2001**, *308* (3), 515−525.
(40) Westermark, P.; Engstrom, U.; Johnson, K. H.; Westermark, G. T.; Betsholtz, C. *Proc. Natl. Acad. Sci. U. S. A.* **1990**, *87* (13), 5036−5040.
(41) Tenidis, K.; Waldner, M.; Bernhagen, J.; Fischle, W.; Bergmann, M.; Weber, M.; Merkle, M. L.; Voelter, W.; Brunner, H.; Kapurniotu, A. *J. Mol. Biol.* **2000**, *295* (4), 1055−1071.
(42) Khemtemourian, L.; Engel, M. F. M.; Liskamp, R. M. J.; Hoppener, J. W. M.; Killian, J. A. *Biochim. Biophys. Acta, Biomembr.* **2010**, *1798* (9), 1805−1811.
(43) Heyl, D. L.; Osborne, J. M.; Pamarthy, S.; Samisetti, S.; Gray, A. W.; Jayaprakash, A.; Konda, S.; Brown, D. J.; Miller, S. R.; Eizadkhah, R.; Milletti, M. C. *Int. J. Pept. Res. Ther.* **2010**, *16* (1), 43−54.
(44) Caillon, L.; Lequin, O.; Khemtemourian, L. *Biochim. Biophys. Acta, Biomembr.* **2013**, *1828* (9), 2091−2098.
(45) Smith, P. E. S.; Brender, J. R.; Ramamoorthy, A. *J. Am. Chem. Soc.* **2009**, *131* (12), 4470−4478.
(46) Knight, J. D.; Miranker, A. D. *J. Mol. Biol.* **2004**, *341* (5), 1175−1187.
(47) Trikha, S.; Jeremic, A. M. *J. Biol. Chem.* **2011**, *286* (41), 36086−36097.
(48) Apostolidou, M.; Jayasinghe, S. A.; Langen, R. *J. Biol. Chem.* **2008**, *283* (25), 17205−17210.
(49) Nanga, R. P. R.; Brender, J. R.; Xu, J. D.; Veglia, G.; Ramamoorthy, A. *Biochemistry* **2008**, *47* (48), 12689−12697.
(50) Pfefferkorn, C. M.; Heinrich, F.; Sodt, A. J.; Maltsev, A. S.; Pastor, R. W.; Lee, J. C. *Biophys. J.* **2012**, *102* (3), 613−621.
(51) Hahl, H.; Möller, I.; Kiesel, I.; Campioni, S.; Riek, R.; Verdes, D.; Seeger, S. *ACS Chem. Neurosci.* **2015**, *6* (3), 374−379.
(52) Marsh, D. *Handbook of Lipid Bilayers*, 2nd ed.; CRC Press, Taylor & Francis Group: Boca Raton, FL., 2013; pp xxvii, 1, 145.
(53) Chazan, A. *Peptide Calculator*, version 1.00; http://biotools.nubic.northwestern.edu/proteincalc.html.
(54) Roux, B. *Comput. Phys. Commun.* **1995**, *91* (1−3), 275−282.
(55) Wolf, M. G.; Jongejan, J. A.; Laman, J. D.; de Leeuw, S. W. *J. Phys. Chem. B* **2008**, *112* (43), 13493−8.
(56) Patil, S. M.; Xu, S.; Sheftic, S. R.; Alexandrescu, A. T. *J. Biol. Chem.* **2009**, *284* (18), 11982−11991.
(57) Nanga, R. P. R.; Brender, J. R.; Vivekanandan, S.; Ramamoorthy, A. *Biochim. Biophys. Acta, Biomembr.* **2011**, *1808* (10), 2337−2342.
(58) Miller, S.; Janin, J.; Lesk, A. M.; Chothia, C. *J. Mol. Biol.* **1987**, *196* (3), 641−656.
(59) Sparr, E.; Engel, M. F. M.; Sakharov, D. V.; Sprong, M.; Jacobs, J.; de Kruijff, B.; Hoppener, J. W. M.; Killian, J. A. *FEBS Lett.* **2004**, *577* (1−2), 117−120.
(60) Junghans, A.; Watkins, E. B.; Majewski, J.; Miranker, A.; Stroe, I. *Langmuir* **2016**, *32* (17), 4382−4391.
(61) Kulikov, O. V.; Kumar, S.; Magzoub, M.; Knipe, P. C.; Saraogi, I.; Thompson, S.; Miranker, A. D.; Hamilton, A. D. *Tetrahedron Lett.* **2015**, *56* (23), 3670−3673.
(62) Kotler, S. A.; Sciacca, M. F. M.; Brender, J. R.; Chen, J.; Yamamoto, K.; Lee, D. K.; Ramamoorthy, A. *Biophys. J.* **2013**, *104* (2), 217a−217a.
(63) Sciacca, M. F. M.; Brender, J. R.; Lee, D. K.; Ramamoorthy, A. *Biophys. J.* **2012**, *102* (3), 488a−488a.
(64) Sciacca, M. F. M.; Kotler, S. A.; Brender, J. R.; Chen, J.; Lee, D. K.; Ramamoorthy, A. *Biophys. J.* **2012**, *103* (4), 702−710.
(65) Lee, D. K.; Brender, J. R.; Sciacca, M. F. M.; Krishnamoorthy, J.; Yu, C. S.; Ramamoorthy, A. *Biochemistry* **2013**, *52* (19), 3254−3263.
(66) Hellstrand, E.; Nowacka, A.; Topgaard, D.; Linse, S.; Sparr, E. *PLoS One* **2013**, *8* (10), e77235.

DOI: 10.1021/jacs.6b06985
J. Am. Chem. Soc. 2017, 139, 137−148